



Regulating the lattice strain field by high-entropy strategy to realize the conformal growth of perovskites for efficient oxygen evolution

Zijin Xu^{a,1}, Zhengyan Du^{a,1}, Runlin Zhang^a, Fanda Zeng^a, Zeshuo Meng^{a,*}, Xiaoying Hu^{b,*}, Hongwei Tian^{a,*}

^a Key Laboratory of Automobile Materials of MOE and School of Materials Science and Engineering, Jilin University, Changchun 130012, China

^b College of Science and Laboratory of Materials Design and Quantum Simulation, Changchun University, Changchun 130022, China

ARTICLE INFO

Keywords:

High-entropy perovskite
Lattice strain field
Conformal growth
Cocktail Effect
Oxygen evolution

ABSTRACT

Perovskite oxides show great promise in the field of water electrolysis due to their low cost and tailorable properties. However, their performance is seriously constrained by crystal agglomeration. Herein, a high-entropy strategy is reported to regulate the lattice strain field, endowing the crystal with a high energy barrier and optimizing its surface properties to achieve conformal growth of highly reactive perovskite oxides. A range of characterization methods and theoretical calculations are used to investigate the lattice distortion-induced complex lattice strain field and the effective activation strategy of the cocktail effect. Based on this, the produced rod-like La(CoFeNiCrAl)O₃ (La5B–Al) exhibits a low overpotential of 285 mV at 10 mA cm⁻² in 1 M KOH. This work provides a novel strategy to use the lattice strain field for regulating the growth of catalysts and clarifies the relationship between high-entropy effects and material properties.

1. Introduction

The oxygen evolution reaction (OER) is a critical aspect in clean energy conversion devices involving electrochemical water splitting [1, 2]. Due to its sluggish kinetics, noble-metal-based catalysts, such as RuO₂ and IrO₂, are typically used to enhance the reaction efficiency [3–5]. However, their application is limited by their high cost and scarcity [6,7]. Thus, the exploration of noble-metal-free-based catalysts, which are both efficient and low-cost, is decisive for the future implementation of large-scale energy conversion technologies.

Among the various noble-metal-free-based catalysts, perovskite oxides (ABO₃) have received widespread attention due to their stability and non-chemometric properties [8–10]. In particular, cobalt-based perovskites (e.g., LaCoO₃) possess an extremely high theoretical intrinsic activity due to their tailorable electronic configuration and abundant ionic valence states [11,12]. However, the high reactivity of their surfaces usually results in a high surface energy, so cobalt-based perovskites typically undergo surface shrinkage to reduce their energy for maintaining a stable structure during growth at high temperatures, which limits the exposure of the active surfaces and slows down the reaction kinetics [13,14]. Thus, the actual OER performance of the

currently developed cobalt-based perovskite electrocatalysts is far below the theoretical predictions [15]. To this end, it is imperative to explore new design strategies to balance their intrinsic activity and exposure area, which could enhance their OER activity to unprecedented levels and promote their large-scale application.

The impressive development of high-entropy materials (HEMs) has brought new solutions to the above problems. Multiple metallic elements form a single-phase solid solution driven by a high configurational entropy (S_{config}), which renders the crystal structure and electronic configuration of HEMs significantly complex, resulting in many unique and novel effects [16–18]. For instance, lattice distortion effects can reduce the surface energy of HEMs through various degrees of structural deformation within the crystal, thereby increasing the exposure of surfaces [19,20]. The cocktail effect induces interactions between elements, which increase the number of oxidation states of surface ions, providing a means to further enhance the OER performance of catalysts [21]. However, the introduction of a high entropy has complicated the system of catalysts, making it difficult to clarify the intrinsic nature of the entropy that balances the properties and performance of catalysts. Therefore, an in-depth exploration of the nature of high-entropy strategies to modulate material properties is necessary to

* Corresponding authors.

E-mail addresses: mengzs21@mails.jlu.edu.cn (Z. Meng), huxy@ccu.edu.cn (X. Hu), tianhw@jlu.edu.cn (H. Tian).

¹ These authors contributed equally to this work.

precisely tailor high-entropy catalysts.

Herein, we used an acidified carbon cloth (ACC) with a good heat resistance as a template to synthesize a series of perovskite electrocatalysts with different configurational entropies through a simple, generalized method. We found anomalies in the growth mode and catalytic activity of the prepared electrocatalysts. By combining experimental characterizations and theoretical calculations, we systematically evaluated the influence of a high entropy on the lattice distortion and electron distribution. This permits us to reveal how the surface physicochemical properties and the growth of the catalysts are regulated by the high-entropy effect. The increased S_{config} at the B-site of perovskite oxides causes severe distortions in the lattice due to ion size mismatch, which renders the strain field inside the crystal more complex. Such a complex strain field results in the crystal nucleus possessing a high energy barrier and an enhanced unloading capacity, thereby reducing the total compressive effect of external stresses at the beginning of nucleation and improving the affinity of the crystal nucleus with the substrate. In addition, the cocktail effect promotes the activation of the metal sites on the perovskite surface, lowers the reaction energy barrier, and improves its intrinsic OER activity. On this basis, we used a high-entropy strategy to regulate the lattice strain field, which permitted us to achieve conformal growth of the oxide crystals along the template, resulting in the first rod-shaped high-entropy perovskites (HEPs) with a high oxygen evolution activity and a high active surface exposure. Additionally, we demonstrated that $\text{La}(\text{CoFeNiCrAl})\text{O}_3$ (La5B–Al), which employs a combination of single-oxidation-state and multi-oxidation-state elements, can more efficiently leverage the interactions between lattice distortions and the cocktail effects to further enhance the catalytic activity of the active sites compared with that of $\text{La}(\text{CoFeNiCrMn})\text{O}_3$ (La5B–Mn), which on the other hand employs only multi-oxidation-state elements. This work provides a new perspective on the use of lattice strain fields to regulate the growth of catalysts, linking high-entropy effects and structure–performance relationships.

2. Experimental section

2.1. Materials

$\text{La}(\text{NO}_3)_3 \cdot 6 \text{H}_2\text{O}$ (99.9%), $\text{Sm}(\text{NO}_3)_3 \cdot 6 \text{H}_2\text{O}$ (99.9%), $\text{Co}(\text{NO}_3)_2 \cdot 6 \text{H}_2\text{O}$ (99%), $\text{Ni}(\text{NO}_3)_2 \cdot 6 \text{H}_2\text{O}$ (98%), $\text{Fe}(\text{NO}_3)_3 \cdot 9 \text{H}_2\text{O}$ (98.5%), $\text{Cr}(\text{NO}_3)_3 \cdot 9 \text{H}_2\text{O}$ (99.99%), $\text{Mn}(\text{NO}_3)_2 \cdot 4 \text{H}_2\text{O}$ (98%), $\text{Al}(\text{NO}_3)_3 \cdot 9 \text{H}_2\text{O}$ (99%), nitric acid (HNO_3), ethanol ($\text{C}_2\text{H}_5\text{OH}$, 95%), potassium hydroxide (KOH, 85%), Nafion (5 wt%), and graphitized carbon black were purchased from Aladdin. All the chemical reagents were used directly without purification.

2.2. Catalyst synthesis

A carbon cloth (CC) with dimensions of $5 \times 6 \text{ cm}^2$ was ultrasonicated in anhydrous ethanol and deionized (DI) water for 30 min to remove organic impurities on the surface. It was then transferred to a glass dish containing concentrated HNO_3 and immersed in a water bath at 55°C for 12 h. After the water bath, the surface was cleaned with DI water three times to remove the residual HNO_3 and dried overnight in an oven at 60°C to obtain an ACC. The ACC has a stronger ion adsorption capacity than CC. 5 mmol $\text{La}(\text{NO}_3)_3 \cdot 6 \text{H}_2\text{O}$, 1 mmol $\text{Co}(\text{NO}_3)_2 \cdot 6 \text{H}_2\text{O}$, 1 mmol $\text{Ni}(\text{NO}_3)_2 \cdot 6 \text{H}_2\text{O}$, 1 mmol $\text{Fe}(\text{NO}_3)_3 \cdot 9 \text{H}_2\text{O}$, 1 mmol $\text{Cr}(\text{NO}_3)_3 \cdot 9 \text{H}_2\text{O}$, and 1 mmol $\text{Al}(\text{NO}_3)_3 \cdot 9 \text{H}_2\text{O}$ were dissolved in 40 mL of anhydrous ethanol. Then, the ACC was soaked in the above solution for 12 h to absorb sufficient ions, and ACC@ions was obtained. Finally, $\text{La}(\text{CoFeNiCrAl})\text{O}_3$ (La5B–Al) was obtained by calcining ACC@ions at 900°C for 3 h at a heating rate of 3°C min^{-1} . Using the same method, other perovskite electrocatalysts can be prepared by simply changing the metal type and proportion of the precursor solution, including LaCoO_3 , LaMnO_3 , $\text{La}(\text{CoFeNi})\text{O}_3$ (La3B), $\text{La}(\text{CoFeNiCrMn})\text{O}_3$ (La5B–Mn), SmCoO_3 , $\text{Sm}(\text{CoCrMn})\text{O}_3$ (Sm3B), and $\text{Sm}(\text{CoFeNiCrMn})\text{O}_3$ (Sm5B).

2.3. Characterization

Thermogravimetric (TG) analysis was performed using a thermal analyzer (STA 449 C, Germany) at a heating rate of $10^\circ\text{C min}^{-1}$. The crystal structure of the catalyst was characterized via X-ray diffraction (XRD, Bruker D8-Advance) with $\text{Cu-K}\alpha$ radiation ($\lambda = 1.5406 \text{ \AA}$). A Thermo Nicolet Nexus 670 FT-IR spectrometer was used for Fourier transform infrared (FT-IR) spectroscopy measurements to detect the bonding of the catalyst. Raman spectra were measured using a laser Raman spectrometer (LabRAM HR Evolution). Scanning electron microscopy (SEM, Hitachi, SU8010) combined with energy-dispersive spectroscopy (EDS), transmission electron microscopy (TEM, FEI Tecnai G2 F20), and high-resolution transmission electron microscopy (HRTEM, FEI Tecnai G2 F20) were used to analyze the morphology and surface element distribution of the samples. The longitudinal thickness of the sample was measured using a white-light interferometer (WLI, ZYGO NewView 5032). The Brunauer–Emmett–Teller (BET) specific surface area and Barrett–Joyner–Halenda (BJH) pore size distributions were obtained via N_2 adsorption/desorption analysis using an ASAP 2020 (Micromeritics, USA). Inductively coupled plasma mass spectrometry (ICP-MS, Thermo-Element XR) was used to quantify the proportion of metal elements in the catalyst. The valence states of the surface elements were analyzed via a X-ray photoelectron spectroscopy (XPS, EscalAB-250, 0.1 eV) using a monochromatic aluminum $\text{K}\alpha$ radiation source.

2.4. Electrochemical measurements

OER electrochemical measurements were performed using a CHI760E electrochemical workstation in a 1 M KOH electrolyte using a standard three-electrode system. Carbon paper with dimensions of $1 \times 1 \text{ cm}^2$ was used as the base of the working electrode. 5 mg of the catalyst and 1 mg of carbon black were mixed in 480 μL of ethanol and 20 μL of Nafion, and the mixture was ultrasonicated for 1 h to obtain a uniform slurry. Then, 150 μL of the slurry was evenly dropped on the carbon paper, which was then placed to dry in an oven to obtain the working electrode with a catalyst loading of 1.5 mg cm^{-2} . An Hg/HgO electrode and a platinum foil were used as the reference electrode and the working electrode, respectively. The linear sweep voltammetry (LSV) curve was recorded at a scanning rate of 5 mV s^{-1} , and the potential was converted to a reversible hydrogen electrode (E_{RHE}) ($E_{\text{RHE}} = E_{\text{Hg/HgO}} + 0.059 \times \text{pH} + 0.098$). Electrochemical impedance spectroscopy (EIS) measurements were conducted in the frequency range of 10^{-1} – 10^5 Hz at an AC amplitude of 10 mV. To measure the double-layer capacitance (C_{dl}), cyclic voltammetry (CV) tests were performed at different sweep rates in the potential window of 1.025–1.125 (V vs RHE). C_{dl} was obtained from the slope of the linear curve at each sweep speed at a voltage of 1.075 V. Thus, the electrochemically active surface area (ECSA) was calculated as $\text{ECSA} = C_{\text{dl}}/C_s$, where $C_s = 0.04 \text{ mF cm}^{-2}$ in alkaline electrolyte [22]. The obtained ECSA was used to normalize the LSV curves to evaluate the intrinsic activity of the catalysts. The cyclic stability of the catalyst was tested at a constant current density of 10 mA cm^{-2} for at least 20 h via chronopotentiometry. The mass activity (MA) and surface area activity (SA) of the catalysts were calculated using the following equations [23]:

$$\text{MA} = j/m, \quad (1)$$

$$\text{SA} = \text{MA}/\text{ECSA}, \quad (2)$$

where j is the current density and m is the catalyst load mass.

2.5. Density functional theory (DFT) calculations

All the density functional theory (DFT) calculations were performed using the Vienna ab initio simulation package (VASP) [24,25]. The Perdew–Burke–Ernzerhof (PBE) [26] exchange–correlation functional and projector augmented wave (PAW) [27] pseudopotential were

adopted with spin polarization. During the structure optimization, the convergence criterion for the total energy was set to 10^{-6} eV, and the atoms were relaxed until the force acting on each atom was less than 0.01 eV/Å. A Gaussian smearing of 0.05 eV was applied to the orbital occupation. A plane-wave cut-off energy of 500 eV was used in all computations. The Brillouin zone was sampled with $3 \times 2 \times 1$ Monkhorst–Pack grids. Each slab model was separated from its neighbors by a 15-Å vacuum layer spacing. The DFT-D3 method of Grimme with a zero-damping function was used for the van der Waals (vdW) corrections [28]. The bulk modulus (K) can be obtained from the Voigt–Reuss–Hill approximation model [29,30]. The free energy profiles, which are useful in estimating the performance of electrocatalytic reactions, were acquired utilizing the computational electrode model (CHE) [31].

The Gibbs free energies of the OER were calculated by correcting the DFT energy with the zero-point energy and entropy according to the following expression:

$$\Delta G = \Delta E + \Delta ZPE - T\Delta S, \quad (3)$$

where E is the DFT total energy, ZPE is the zero-point energy, T is the environment temperature, and S is the entropy. For the ZPE correction and entropy calculations, the vibrational frequencies were calculated by employing the density functional perturbation theory.

2.6. Molecular dynamics (MD) simulations

Molecular dynamics (MD) simulations and geometry optimizations of the molecular chain models were performed using the Forcite module of the Materials Studio 2020 software package. The molecular structures of the compounds were built using the Materials Visualizer module with application of the Universal force field throughout. To equilibrate these systems, NVT dynamics followed by 5000-ps NPT dynamics were used for each system, where the number of particles N , volume V , pressure P , and temperature T in the system were all held constant. The temperature was kept constant at 574 K, and all simulations were conducted for 1×10^7 steps for a total time of 10000 ps. As shown, both energy and temperature were very stable at 574 K after dynamic simulations for 10000 ps, which indicates the high stability of the structures. Additionally, the binding energy (E_b) was calculated according to the following expression:

$$E_b = E_{A+B} - E_A - E_B \quad (4)$$

Here, E_A represents the metal oxide molecular, E_B represents the adjacent carbon nanotube or another metal oxide molecular, and E_{A+B} is the total energy of both parts.

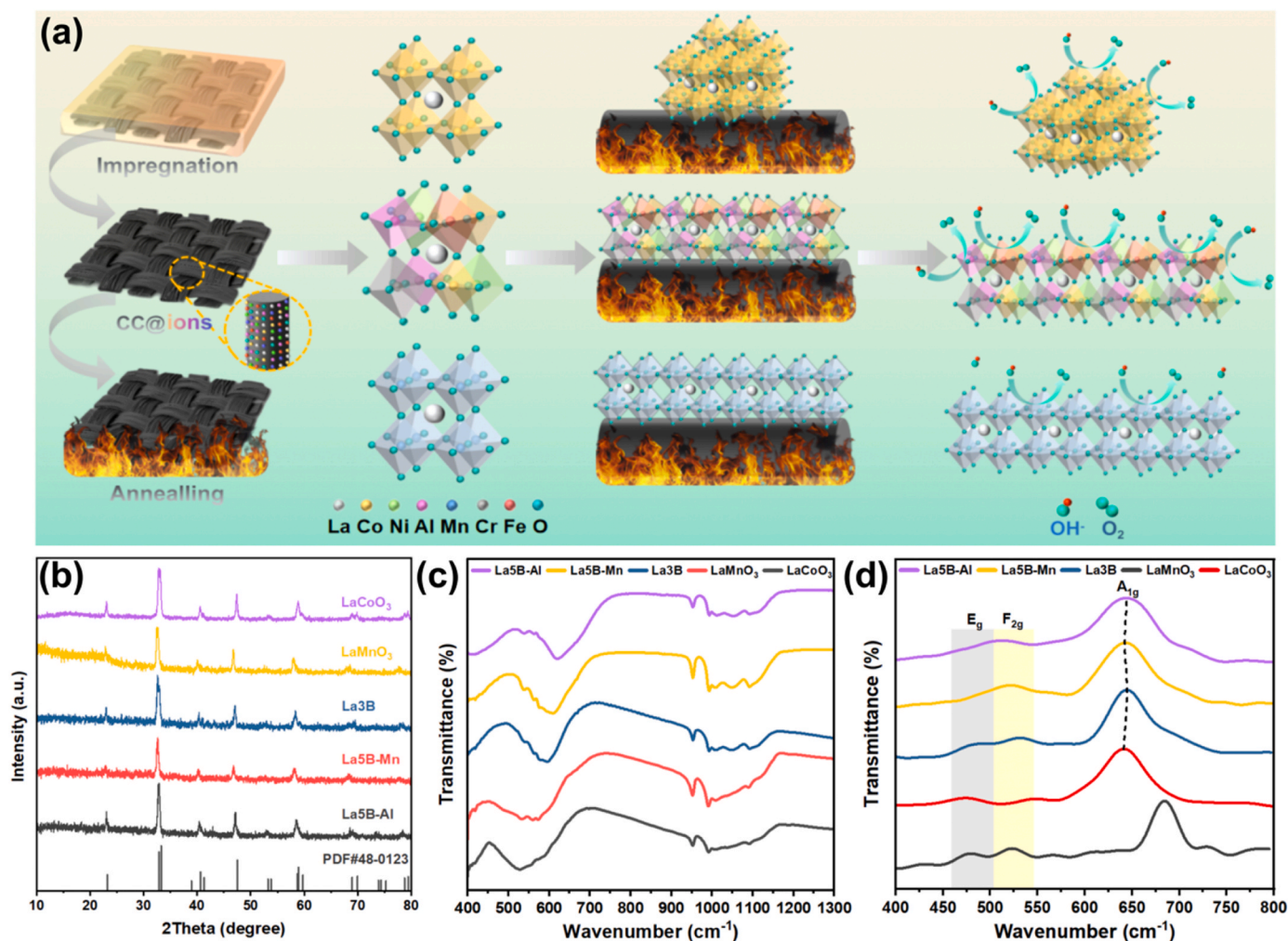


Fig. 1. a) Schematic of the synthesis and differences in the growth mode and catalytic activity of the investigated perovskite oxides. b) XRD patterns, c) FT-IR spectra, and d) Raman spectra of the different perovskite oxides.

3. Results and discussion

3.1. Structural characterization of the catalysts

The perovskite catalysts were synthesized using a simple impregnation-annealing method (Fig. 1a and Fig. S1, Supporting Information). The hydrophilized ACC was first immersed in an alcoholic solution of metal nitrates for 12 h. Subsequently, the ACC, fully adsorbed with metal ions, was annealed in air at 900 °C for 3 h to remove the template and collect the powder. The formation of chalcocite was tracked using thermogravimetric analysis-derivative thermogravimetric analysis (TGA-DTG). As shown in Fig. S2 (Supporting Information), the TG curve of the CC shows only two heat absorption peaks. At 600 °C–800 °C, the carbon fiber starts to melt and the oxygen-containing functional groups on the surface decompose. At above 800 °C, the carbon fiber starts to rapidly oxidize and decompose. After impregnation, the TG curve of the ACC shows more thermal absorption peaks. The peak at around 100 °C represents the loss of surface water. Since nitrate ions can provide an oxidizing environment, the temperature at which the ACC surface oxidizes is increased (400 °C–650 °C) and the intensity of the absorption peak is reduced [32]. The peak corresponding to this process is broadened compared with that of the CC, which indicates that the metal ions have started to crystallize and nucleate. Subsequently, the high-entropy oxides grow rapidly, and the growth is finished at 725 °C. At 725 °C–800 °C, the templates are removed to a greater extent. Since the formation of HEPs usually requires high temperatures, it is difficult to use conventional templates for tailoring the morphology of HEPs. ACC, on the other hand, exhibits better temperature tolerance than other reported templates, offering the possibility to support the conformal growth of HEPs.

By modulating the type and proportion of metal ions in the precursor solution, it becomes feasible to customize perovskite oxides with different S_{config} values. To verify the widespread applicability of the proposed synthesis strategy, five La-based perovskites, namely LaCoO₃, LaMnO₃, La₃B, La₅B–Mn, and La₅B–Al, were successfully prepared. Considering the possible effect of the increased B-site element species on the thermodynamic stability of the perovskites, the structural tolerance factor (t) and the ionic radius difference (δ) of the HEPs were calculated, and the results are consistent with the requirements for structural stability (Table S1, Supporting Information). The XRD patterns in Fig. 1b show that the synthesized samples are all single-phase perovskite oxides (their patterns match that of LaCoO₃, PDF#48-0123) with the carbon fiber template removed, and no additional diffraction peaks are observed. It is worth noting that the (110) diffraction peak near 33° shifts to a lower angle when the Co³⁺ ions are partially substituted by other ions, i.e., Cr³⁺, Mn³⁺, Fe³⁺, and Ni³⁺, which indicates the expansion (distortion) of the original lattice due to the increased average ionic radius at the B-site [33,34]. Since the Al³⁺ radius is much smaller than that of the transition metal element, the average ionic radius increase of La₅B–Al is the lowest and the offset of the (110) diffraction peak is the smallest. On the other hand, LaMnO₃ has the largest increase in the average ion radius and the largest shift of the peak, followed by those of La₅B–Mn and La₃B. The lattice parameters of each catalyst were obtained from the Rietveld refinement of the XRD patterns (Fig. S3 and Table S2), and the results confirm the lattice expansion due to element substitution at the B-site, which is consistent with the above analysis. Alongside the lattice expansion, the more B-site elements are added, the greater the ion size mismatch within the lattice becomes, which renders the lattice strain field more complex and leads to unique new properties [35].

FT-IR spectroscopy further demonstrates the bonding changes of the catalysts (Fig. 1c). The spectra are essentially the same for the different samples. The absorption peaks in the high-wavelength band near 1000–1100 cm^{−1} are attributed to the vibration of the perovskite lattice [36–39]. The large vibrational peak in the low-wavelength band can be split into three peaks. The peak near 550 cm^{−1} corresponds to the

O–B–O bending vibration in the BO₆ octahedron; the peak near 590 cm^{−1} represents the B–O–B symmetric vibration in the BO₆ octahedron; the peak near 625 cm^{−1} represents the B–O asymmetric vibration. The results show that the intensity of the asymmetric vibrational band gradually increases as the S_{config} of the B-site increases, which leads to a shift in the peak position toward a higher wave number [22,40]. This again indicates that the HEPs undergo lattice distortion, and the B–O bond lengths in the octahedra change, resulting in a lower symmetry of the electron distribution, which contributes to improving the OER activity of the electrocatalyst [40,41]. Raman spectroscopy was carried out to further explore the properties of the bonds in the perovskite oxides to gain a better understanding of the lattice expansion. The Raman spectra of all catalysts (Fig. 1d) can be deconvoluted into three peaks, namely the E_g peak (~470 cm^{−1}), F_{2g} peak (~525 cm^{−1}), and A_{1g} peak (~650/680 cm^{−1}), further confirming the single-phase structure of the perovskites. The F_{2g} and A_{1g} peaks are attributed to the symmetric and antisymmetric vibrations of the B–O bonds in the BO₆ octahedron, respectively [42–44]. With the increase in the configurational entropy, the structure disorder and lattice distortion shorten the average lifetime of the phonons in the crystal, leading to the weakening and broadening of the Raman peaks, in which the E_g and F_{2g} peaks are merged into a broader peak [45]. In addition, the A_{1g} vibration band is closely related to the length of the B–O bond. In particular, the A_{1g} vibration band (~680 cm^{−1}) of LaCoO₃ is significantly redshifted compared with that of the other perovskites (~650 cm^{−1}), indicating that LaCoO₃ has the shortest B–O bond length [46]. The relative position of the A_{1g} peak for the other samples is roughly consistent with the degree of lattice expansion determined by the XRD patterns. The FT-IR and Raman characterization results show that the lattice distortion may depend more strongly on the change in the B–O bond when the B-site configurational entropy is adjusted.

The morphology and structure of all samples were observed via SEM and TEM (Fig. 2a–o). Interestingly, LaCoO₃ shows a distinct growth mode from that of the other catalysts, with particularly severe agglomerations and a greater bulk thickness. The growth of the other perovskites is more uniform and the regular nanorod-like morphology is maintained. The grain size is an important factor for comparing the tendency and extent of agglomeration of different perovskites. The grain size of each perovskite was extracted from the SEM images (Fig. S4, Supporting Information). The results show that LaCoO₃ has the largest mean grain size among the perovskites after a given annealing process, which indicates that its grains are more prone to grow through ripening. A quantitative classification of the morphological differences was conducted using a WLI, and the results show that the thickness of most catalysts ranges from 600 to 900 nm, while the thickness of the cobalt-based single perovskite is roughly double (Fig. S5, Supporting Information). The BET and BJH methods were used to evaluate the specific surface area and pore size distribution of each catalyst (Fig. S6, Supporting Information). The surface area and average pore size of LaCoO₃ are both low because of severe agglomeration, and the conformal growth of the other catalysts effectively ensures a good surface exposure (Table S3, Supporting Information). The high-resolution TEM (HRTEM) images confirm the single-phase structure of the catalysts (Fig. 2p–t and Fig. S7, Supporting Information). The (110) plane spacing of LaCoO₃, LaMnO₃, La₃B, La₅B–Mn, and La₅B–Al is 0.265, 0.278, 0.273, 0.276, and 0.272 nm, respectively. The trend of these values is consistent with that of the offset of the peak of the (110) plane in the XRD patterns, which once again proves the lattice expansion caused by the incorporation of the different B-site elements. Being the most significant difference between the various samples, lattice distortion may be a plausible explanation for the observed differences in the growth behavior. EDS mappings (Fig. 2u–y) confirm the uniform distribution of the elements in the samples without any second-phase segregation. In addition, the concentration of metal elements in each HEP was determined using ICP-MS (Table S4, Supporting Information). The proportion of B-site metal elements in the HEPs is close to the equal molar ratio, and

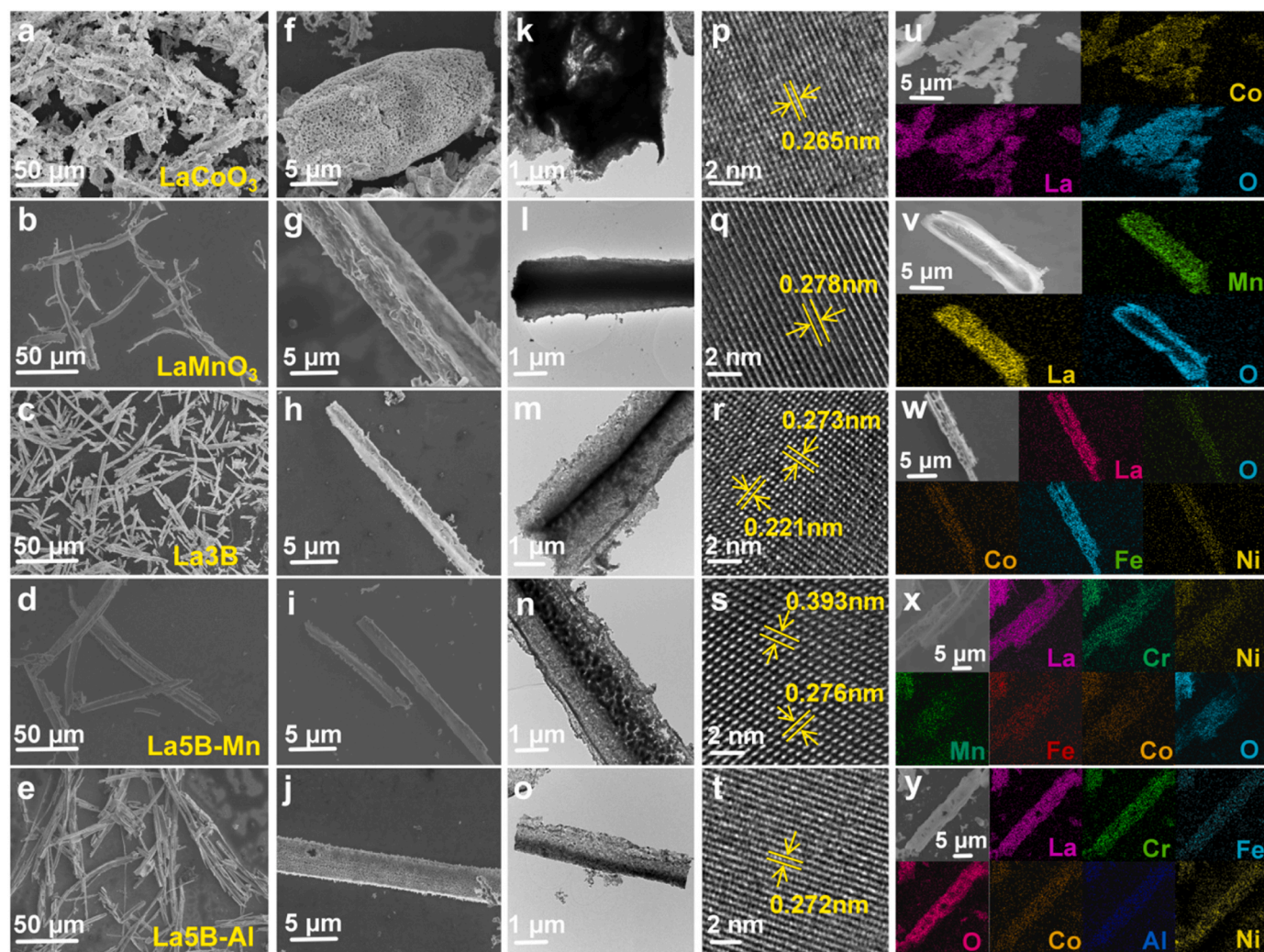


Fig. 2. a–j) SEM images, k–o) TEM images, p–t) HRTEM images, and u–y) SEM images with corresponding EDX elemental mappings of LaCoO₃, LaMnO₃, La₃B, La₅B–Mn, and La₅B–Al.

the calculated S_{config} is in the range of 1.60–1.61 R (i.e., greater than 1.55 R), which is in line with the expectations of HEP synthesis [21].

3.2. OER performance measurement

The OER performance of the perovskite electrocatalysts was evaluated in a 1 M KOH electrolyte using a standard three-electrode system, and the potential was calibrated to an RHE. Commercial RuO₂ was used as a reference. As shown in Fig. 3a, the HEPs exhibit a significantly lower overpotential (η_{10}) than the other electrocatalysts at a current density of 10 mA cm⁻². In particular, La₅B–Al has the lowest overpotential (285 mV), which is superior to that of many reported perovskite electrocatalysts (Table S5, Supporting Information). The Tafel diagram (Fig. 3b) was obtained based on the LSV curves to evaluate the OER kinetics of each catalyst. The Tafel slopes of La₅B–Al, La₅B–Mn, La₃B, LaMnO₃, LaCoO₃, and RuO₂ were 95.44, 100.20, 125.06, 150.16, 157.44, and 105.86 mV dec⁻¹, respectively. The charge-transfer resistance (R_{ct}) of these catalysts was measured via EIS. As shown in Fig. 3c and Table S6 (Supporting Information), the R_{ct} values of the samples followed the same trend as their Tafel slopes; the smaller R_{ct} values of the HEPs indicate that they have a greater OER charge transfer capability. Notably, LaCoO₃, which has a relatively high catalytic activity, exhibits the slowest OER kinetics, which is attributed to the fact that the severe agglomeration leads to the existence of few exposed active sites and a poor surface conductivity, thus severely limiting its intrinsic

catalytic activity. Subsequently, the C_{dl} of the samples (Fig. 3d) was calculated from the CV curves recorded at different scanning rates (Fig. S8, Supporting Information). The estimated ECSA values of La₅B–Al, La₅B–Mn, La₃B, LaMnO₃, LaCoO₃, and RuO₂ were ~71, ~58, ~47, ~45, ~31, and ~54 cm², respectively, which again confirm the above speculations. To compare the intrinsic activity of the different catalysts more accurately, the ECSA-normalized LSV curves were plotted (Fig. 3e), and the results show that the intrinsic catalytic activity obeys the following trend: La₅B–Al > La₅B–Mn > LaCoO₃ > La₃B > RuO₂ > LaMnO₃. The HEPs were observed to maintain a relatively high activity, which indicates that the observed variation in the OER performance is not only due to the increased surface area but also to the increase in the intrinsic activity of the catalyst. However, the activity ranking of LaCoO₃ is elevated, which again demonstrates the negative effect of aggregation on the catalyst in exerting its intrinsic activity. In order to compare the performance indexes of the various catalysts more comprehensively and intuitively, we calculated and compiled the overpotential at a current density of 10 mA cm⁻² (η_{10}), Tafel slope, C_{dl} , ECSA, MA ($\eta = 400$ mV), and SA activity ($\eta = 400$ mV) of each catalyst. As shown in Fig. 3f and Table S7 (Supporting Information), each performance index of La₅B–Al is excellent. To further confirm the potential application value of La₅B–Al, a chronopotentiometry test was performed at a current density of 10 and 100 mA cm⁻² (Fig. S9, Supporting Information); it can be observed that its activity did not change significantly after more than 20 h of continuous testing. Through the above

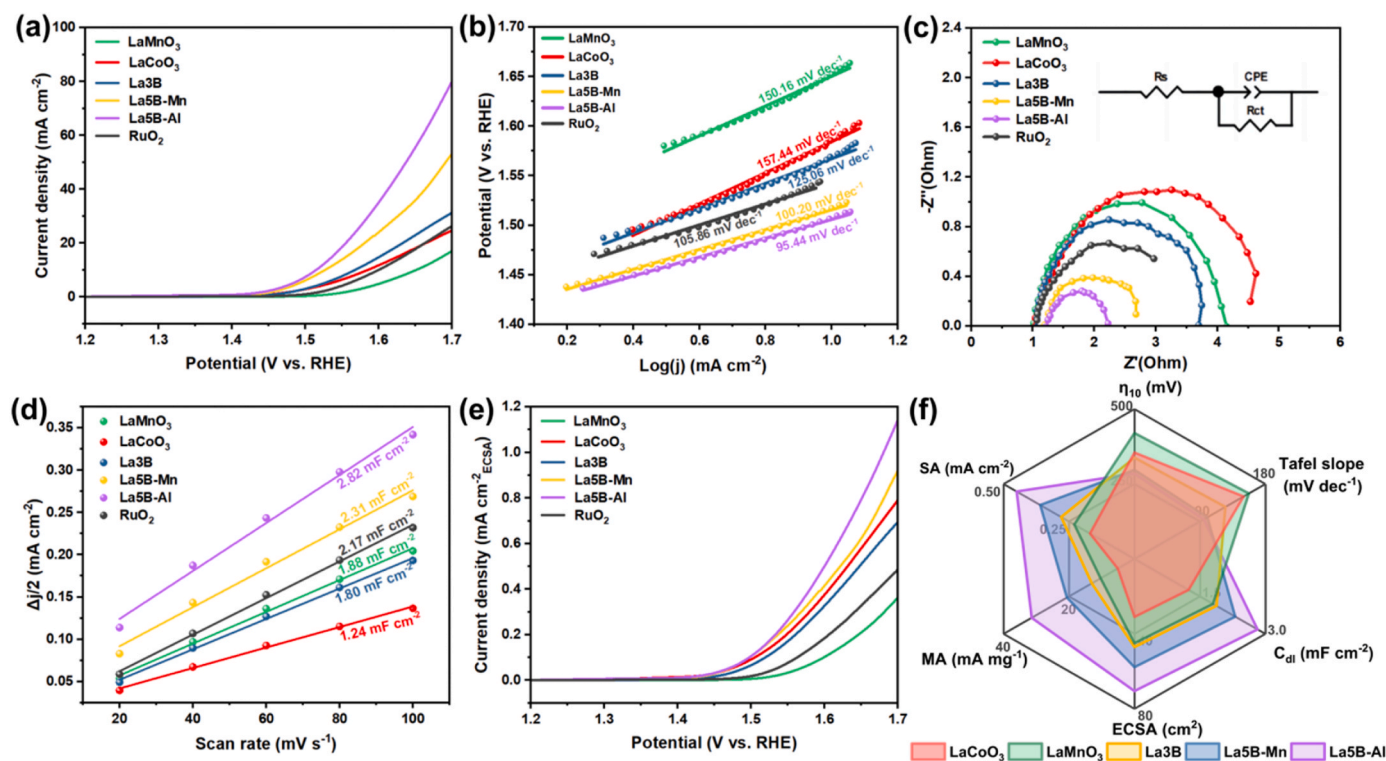


Fig. 3. a) LSV curves at 10 mA cm⁻², b) Tafel slopes, c) Nyquist plots, d) charging currents at 1.075 V (vs RHE) as a function of the scan rate, e) LSV curves normalized to the ECSA, and f) comparison chart of the OER performance indicators of the different catalysts.

characterization measurements and performance evaluation, we found that LaCoO₃ with a high intrinsic activity shows greater OER performance compared with nanorod-like LaMnO₃ despite its severe agglomeration. However, the introduction of the entropy effect in the catalyst not only improves the basic OER activity but also maintains the growth characteristics of LaMnO₃. Therefore, further investigation of the possible relationship between the entropy effect and the structure–growth–performance can provide a better understanding of how materials are improved by utilizing a high-entropy strategy.

3.3. Entropy effects on crystal growth

The growth pattern of nanoparticles (NPs) on the substrate is closely related to the physicochemical properties of the surface at the initial stage of nucleation. In general, if the surface energy of an NP is high, it tends to reduce its energy through agglomeration to maintain stability, but this will also inhibit the catalytic activity of its surface [47]. In addition, the wettability between the NP and the substrate significantly affects its growth mode [48,49]. Exploring the possible relationship between the entropy effects and the crystal structure as well as the growth mode requires further analysis of the nucleation–growth process of perovskites.

To this end, DFT and MD were used to simulate LaCoO₃ and La5B–Al. Firstly, with the help of the DFT, the tuning effect of entropy on the lattice was clarified theoretically. An increase in the B-site element species is usually accompanied by changes the B–O bond, which causes a rebalancing of the electron density and leads to elastic deformation of the lattice [50]. As shown in Fig. 4a and b, compared with the LaCoO₃ charge density difference results, the electron cloud of La5B–Al is broadened and tends to be delocalized overall. The relative position of the ions also changes significantly, which proves the occurrence of lattice distortion. The electron localization function (ELF) more clearly shows the change in the electron cloud distribution (Fig. 4c and d), and the symmetry of the electron cloud of La5B–Al is significantly reduced, which is consistent with the charge density differences. In addition, the

XRD and HRTEM results have revealed that LaCoO₃ has the smallest lattice parameters and lattice expansion can be achieved by adjusting the B–O bond, which is consistent with the average bond length obtained via the DFT calculations (Table S8, Supporting Information). The dominant effect of the B–O bond diversification on lattice expansion is confirmed again.

Then, the possible relationship between the lattice expansion and the surface energy induced by the entropy effect was analyzed. It is difficult to directly characterize the surface energy of oxide nuclei at the early nucleation stage, so we qualitatively analyzed the surface tension (γ), which has the same physical significance. In the classical theory of solid state physics, γ arises from the imbalance of forces on the surface of a solid, and the greater the degree of imbalance, the greater the value of γ . In crystal nucleation, ions are bonded to each other via the Coulomb interaction, and the overall Coulomb interaction is attractive despite the repulsion between ions with the same charge sign. Subsequently, the accumulated ions gradually reduce in size under the action of external pressure (atmospheric pressure and γ) to form a protocell. The larger the total ion attraction and external force, the smaller the lattice parameters of the protocell [51,52]. Therefore, the Coulomb attraction between the ions of LaCoO₃ with a small lattice is greater and γ is larger at the early nucleation stage. As the B-site S_{config} increases, lower-atomic-number elements gradually replace Co, which weakens the Coulomb attraction and surface tension between the ions and slows down grain agglomeration. The MD simulations also confirm this hypothesis (Fig. 4k and l). The self-aggregation energy between LaCoO₃ modules ($E_{s1} = -0.24$ eV) is six times that between La5B–Al modules ($E_{s2} = -0.04$ eV), indicating that LaCoO₃ is more prone to undergo thermodynamic aggregation [53].

Furthermore, the influence of entropy on wettability is discussed. The wettability between the oxide NP droplet and the template surface is related to the degree of affinity between them, which is manifested in the difference in the contact angle on a macroscopic level. In the process of ion accumulation and binding, external forces such as γ , continuously compress the ion cluster until they reach equilibrium with the repulsive force inside the cluster. In the theory of solid-state physics, the bulk

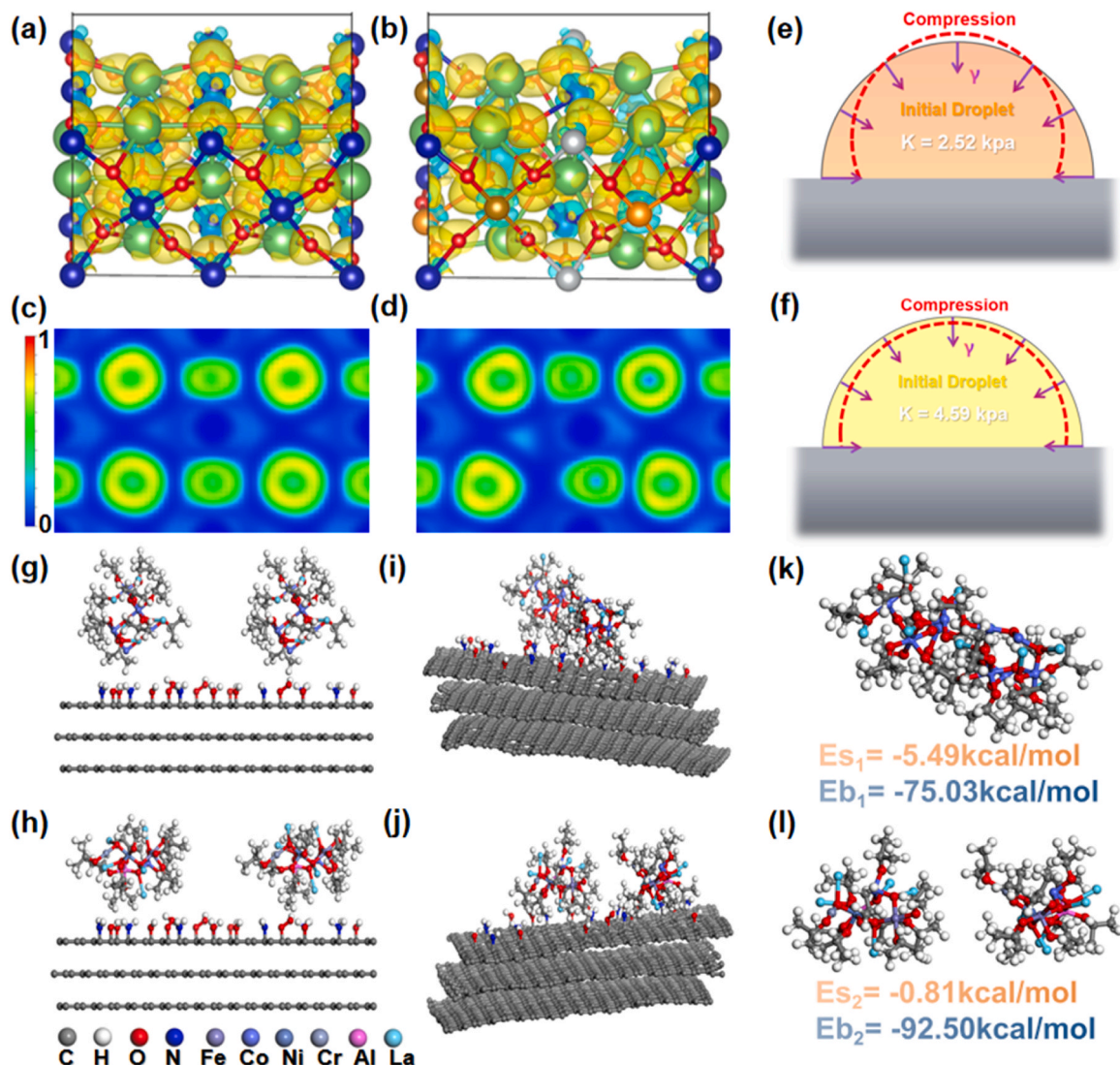


Fig. 4. a) and b) Charge density differences, c) and d) electron localization function, and e) and f) schematic of the effect of different K values on the surface wettability of LaCoO₃ and La5B-Al. MD simulations of the growth process of (g), (i), and (k) LaCoO₃ and (h), (j), and (l) La5B-Al.

modulus (K) is typically used to measure the magnitude of this repulsive force [51,52], so the value of K can be used to qualitatively compare the contact angle differences. The lattice distortion caused by the high entropy makes the lattice stress field more complex and disordered so that the unloading capacity inside the crystal is enhanced, thus improving its resistance to external stress and reducing the total effect of compression [54]. The DFT calculations show that the K value of La5B-Al (4.59 kPa) is nearly twice that of LaCoO₃ (2.52 kPa). Therefore, La5B-Al theoretically has a small contact angle and a strong affinity with the substrate (Fig. 4 f). LaCoO₃, on the other hand, has a larger contact angle and a weaker affinity with the substrate (Fig. 4e), which is why it exhibits more pronounced migration and agglomeration [49]. In addition, the adsorption energy (E_{b1}) of LaCoO₃ on the template surface is only -3.25 eV, which is lower than that of La5B-Al ($E_{b2} = -4.01$ eV), further confirming the poor affinity between LaCoO₃ and the template. The MD simulations more clearly show the difference in the dynamic behavior between LaCoO₃ and La5B-Al in the sintering process. During the simulation period of 10000 ps, the structure of the two systems remains stable (Fig. S10, Supporting Information). The simulation results show that LaCoO₃, which is characterized by a higher surface energy and a stronger affinity, exhibits evident self-aggregation (Fig. 4i), while La5B-Al, which possesses a lower surface energy and a stronger affinity,

remains uniformly attached to the template surface without clear diffusion (Fig. 4j).

In summary, LaCoO₃ nuclei with a high intrinsic activity have a poor ability to resist compression under a high surface tension and cannot maintain a good affinity with the substrate; thus, agglomeration during growth severely limits the intrinsic activity. For La5B-Al, the increase in the B-site S_{config} values is accompanied by a differentiation of the B-O bonds, which causes severe lattice distortion and renders the strain field inside the crystal more complex. This results in the crystal nucleus having a high energy barrier, which reduces the effect of external stress on the crystal nucleus and improves its wettability with the substrate, ensuring the conformal growth of the crystals and the importance of the intrinsic activity. Regarding the less active LaMnO₃, the B-O coupling is weaker and the surface energy is certainly lower, so the total compression due to the Coulomb interaction and γ is doubtlessly smaller. In this case, even if the lattice strain field is small, it can maintain a good affinity with the substrate and thus achieve conformal growth. Nevertheless, the activity of LaMnO₃ remains poor, as it is determined by its low intrinsic activity. This further elucidates the structure-performance relationship that exists between the morphology and intrinsic activity of perovskites. It should be noted that this entropy regulation strategy can also be applied to other perovskite systems. In the XRD diffraction

pattern of the synthesized Sm-based perovskites (Fig. S11 Supporting Information), a negative peak shift caused by lattice expansion is also observed. The SEM images (Figs. S12–S14, Supporting Information) show that SmCoO_3 also undergoes agglomeration. With the increase in the B-site element species, the samples also transform into nanorods. This again confirms the widespread applicability of our synthesis method and control strategies.

3.4. Entropy regulation of the OER activity

In addition to the possible influence on the growth mode, the unique effect of the high entropy on the catalyst also provides the possibility to improve the intrinsic OER activity of perovskites [55]. For example, tensile lattice strain can result in the catalyst reaching a thermodynamic nonequilibrium state, thus enhancing the adsorption capacity of the reaction intermediates. The cocktail effect causes the electrons to migrate between the active metal elements. The migration path is generally related to the relative electronegativity of the elements. The greater the electronegativity, the easier it is to attract extra electrons [56]. In this case, the transition metal may change its oxidation state and spin state, which will also affect the overlapping degree of the metal 3d orbital and the oxygen 2p orbital, endowing the catalyst with new properties [57]. However, performance differences between La5B–Al and La5B–Mn were observed, indicating that the synergistic effects between different element combinations are not the same. Therefore, it is crucial to further clarify the details of the regulation of the entropy effect on materials for the exploration and prediction of high-entropy catalysts.

The valence difference of the active elements on the surface of the

perovskite catalysts was analyzed via XPS. The O 1s spectrum can be deconvoluted into four peaks: lattice oxygen (O_I) at ~ 529.0 eV, oxygen void (O_II) at ~ 530.3 eV, adsorbed oxygen (O_III) at ~ 533.2 eV, and surface adsorbed water (O_IV) at ~ 533.6 eV (Fig. 5a) [58]. Surface oxygen vacancies can enhance the charge density near the Fermi level to promote interfacial electron transfer, thus improving the activity of the catalyst [59], which may interfere with the investigation of the entropy effects on the regulation of the electronic structure and activity of the catalyst. The percentages of oxygen species extracted from the XPS data show that the percentages of O_II in different catalysts are similar (Table S9, Supporting information), eliminating the effect caused by oxygen defects. As shown in Fig. 5b, the two main peaks in the Co 2p spectrum are located near 780.2 and 795.5 eV and correspond to Co $2p_{3/2}$ and Co $2p_{1/2}$, respectively. Further deconvolution yields Co^{3+} (~ 779.4 and ~ 794.7 eV) and Co^{2+} (~ 781.0 and ~ 796.3 eV) [60]. The peak at 775.7 eV is the Auger electron peak of Co [61]. The peaks at 789.8, and 804.7 eV are satellite peaks [62]. The Fe 2p spectrum (Fig. 5c) can be deconvoluted into five peaks: the Fe^{2+} peaks are located at 709.5 eV (Fe $2p_{3/2}$) and 722.7 eV (Fe $2p_{1/2}$), the Fe^{3+} peaks are located at 711.4 eV (Fe $2p_{3/2}$) and 724.6 eV (Fe $2p_{1/2}$), and the remaining peak is a satellite peak [63]. With increasing configurational entropy, the binding energies of the Co 2p and Fe 2p peaks both shift toward higher values, which indicates an increase in their average valence. The Co sites in higher valence states are more covalent with lattice oxygen and are more capable of adsorbing the oxygen intermediates [64]; furthermore, the Fe in the high oxidation states act as redox cooperative centers to enhance the oxidizing ability of the Co site [65]. The specific ratio between the valence states of the elements obtained from the XPS data also confirms the increase in the Co and Fe

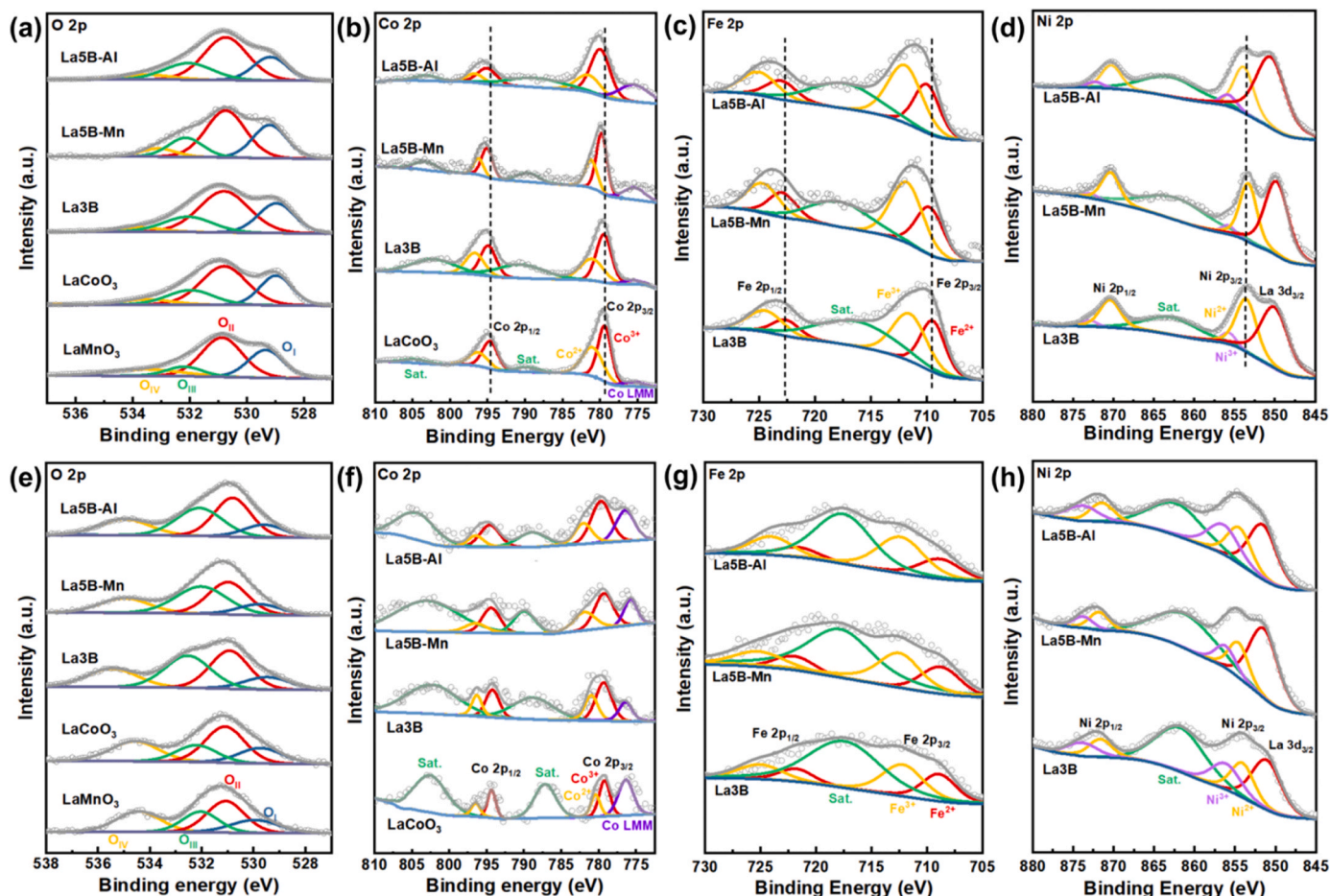


Fig. 5. High-resolution XPS spectra of each catalyst (a)–(d) before and (e)–(h) after cycling for (a, e) O 1s, (b, f) Co 2p, (c, g) Fe 2p, and (d, h) Ni 2p.

oxidation states (Table S9, Supporting information). In the Ni 2p spectrum (Fig. 5d), the Ni^{2+} peaks are located at 853.9 eV (Ni 2p_{3/2}) and 871.5 eV (Ni 2p_{1/2}), the Ni^{3+} peaks are located at 856.0 eV (Ni 2p_{3/2}) and 874.2 eV (Ni 2p_{1/2}), and the satellite peak is located at 862.1 eV, with a strong La 3d_{3/2} peak near 851.2 eV [62]. Due to its strong electronegativity, Ni usually acts as an electron acceptor, so its oxidation state in La5B–Mn doped with more species with a low electronegativity is lower than that in La3B. Therefore, the binding energy of the Ni^{2+} peak of La5B–Mn is small and the value of $\text{Ni}^{3+}/\text{Ni}^{2+}$ is only 0.13 (Table S9, Supporting information). This limits the catalytic performance of Ni as a potential active site to some extent. Interestingly, the Ni in La5B–Al does not act as an electron acceptor as expected. The binding energy of its Ni^{2+} peak is slightly increased rather than decreased, as observed for La5B–Mn, which implies that the effects induced by different element combinations are not the same. This may be because to improve the stability of the system, the HEPs in the metastable state tend to spontaneously reduce the δ value to decrease the extra energy associated with lattice distortion. The valence states of Mn elements in La5B–Mn are abundant, so above purpose can be achieved by adjusting the proportion of Mn ions in different valence states. Therefore, the presence of Mn^{2+} is observed in the Mn 2p spectrum of La5B–Mn compared to LaMnO_3 (Fig. S15b, Supporting Information). However, the monovalent state of Al greatly reduces the tunability of the lattice distortion degree. In this case, the system will force further electron migration between other metal elements, especially those with numerous different valence states, to release as much extra energy as possible. For this reason, Ni^{2+} with a larger ionic radius tends to lose more electrons, thus restraining the attraction of electrons due to its high electronegativity, keeping the oxidation state of Ni in La5B–Al at a relatively high level or even slightly increased. Additionally, the ability of Cr^{6+} to attract electrons is further activated, so the content of Cr^{6+} in La5B–Al is significantly lower than that in La5B–Mn (Fig. S15c, Supporting Information). This provides a new perspective for the reasonable collocation of B-site elements in HEPs. For inactive sites, the selection of metal elements with monovalent states that can provide greater distortion within the range of structural tolerance may stimulate better synergy between the active sites, resulting in a superior performance.

To further analyze the differences in the performance between the various perovskites, we collected the samples after 1 h of continuous operation at a current density of 10 mA cm^{-2} and detected the changes in the phase and surface chemical states after cycling. As shown in Fig. S16 (Supporting Information), the XRD diffraction peaks of the perovskites widened because of the amorphous surface. Except for the spinel-phase segregation observed in LaCoO_3 , the other catalysts maintained their original structure. The SEM images and EDS mapping results show that the morphology of the catalysts changed only slightly before and after the OER, and the distribution of the elements was still uniform (Figs. S17 and S18). The XPS results after the OER reveal that all elements in the catalyst were retained (Fig. 5e–h). In the O 1s spectrum, the peaks corresponding to surface-adsorbed oxygen (O_{III}) and surface-adsorbed water (O_{IV}) are significantly enhanced. The retention of lattice oxygen (O_{I}) indicates that the main perovskite structure is preserved after cycling. Due to the influence of the amorphous surface, the proportion of oxygen vacancies increases, which qualitatively indicates an increase in the number of available active sites for the OER [57]. At the same time, the peaks of the active elements Co 2p, Fe 2p, and Ni 2p shift toward higher binding energies after the OER, and the ratio of higher to lower valence ions increases further (Table S10, Supporting Information). This indicates that active ions in higher valence states are produced during the catalytic process. These ions facilitate the optimal filling of the surface transition metals to maintain an efficient OER process [66]. It is noteworthy that the Ni^{3+} content in La5B–Al after cycling is significantly higher than that in La5B–Mn, which again confirms the excitation effect of monovalent Al on the active sites. The Mn and Cr valences decreased after cycling, and these two elements mainly contributed to stabilizing the crystal structure (Fig. S19, Supporting

Information).

The electron structure and activity sources of the catalysts were studied via DFT. XPS analyses revealed that Fe, Co, and Ni in high-entropy catalysts were effective active sites for the OER. The calculated adsorption energy of these sites in La5B–Mn and La5B–Al for oxygenated intermediates shows that the Co site has the highest adsorption capacity for each intermediate, and thus it is the site that can most easily serve as a catalytic site (Fig. S20). Therefore, the catalytic properties of the Co sites in LaCoO_3 , La5B–Mn, and La5B–Al were compared theoretically to further analyze the proposed high-entropy strategy for improving the OER performance. The calculated total density of states (TDOS) (Fig. 6a) shows an increase in the spin states near the Fermi level (E_{f}) of La5B–Mn and La5B–Al, indicating that more electrons accumulate near the E_{f} , which enhances the semi-metallic properties of the catalyst and provides good conduction support for the reaction [67–69]. The d-band centers of Co 3d were compared in terms of the partial density of states (PDOS) (Fig. 6b). The d-band center of La5B–Al (–1.268 eV) is closer to the E_{f} than the d-band centers of La5B–Mn (–1.283 eV) and LaCoO_3 (–1.407 eV); thus, La5B–Al has the optimal ability to bind oxygen intermediates [70]. Based on the characterization results, the reaction processes of the oxygen-containing intermediates (*OH , *O , and *OOH) at the active Co site were further calculated using the (110) plane as models (Fig. 6c and Fig. S21, Supporting Information). As shown in Fig. 6d, the capacity of each catalyst to adsorb intermediates obeys the following trend: La5B–Al > La5B–Mn > LaCoO_3 , which is consistent with the PDOS prediction results. The above results indicate that La5B–Al adsorbs oxygen-containing groups with lower energy barriers for a faster proton–electron transfer process [71]. In addition, the Gibbs free energy (ΔG) calculations for the oxygen-containing intermediates at each step of the OER process (Fig. 6e) show that the rate-determining step (RDS) for all three reactions is the formation of *OOH . As La5B–Al has a strong ability to adsorb *OOH , its RDS has the lowest ΔG (Fig. 6f) and theoretically exhibits better OER activity, which is consistent with the experimental results.

4. Conclusion

In conclusion, the crystal structure, electron distribution, and surface properties of perovskites were effectively regulated by a high-entropy strategy. Through different characterization methods, DFT calculations, and MD simulations, it was found that the effect of the lattice distortion regulation on the lattice strain field endows La5B–Al with a large bulk modulus (4.59 kPa), which enhances the unloading capacity of the crystal nuclei, reduces the total effect of volume reduction, and improves the affinity with the substrate. Additionally, the difference in the growth process of the catalysts was visually confirmed through MD simulations. A nanorod-like La5B–Al was prepared as a proof-of-concept system; it exhibited a low overpotential of 285 mV at a current density of 10 mA cm^{-2} in 1 M KOH. The influence of the cocktail effect on the oxidation state of the surface active metal sites was systematically analyzed, and the reason behind the excellent OER performance of HEPs was clarified. Based on these findings, a high-entropy catalyst design strategy was proposed, which uses inactive elements with a single oxidation state to increase the lattice distortion and drive a more efficient cocktail effect to activate the active sites. This study explores effective approaches to regulate the growth mode and surface physico-chemical properties of catalysts using high-entropy strategies, opening up new dimensions for clarifying the impact of high-entropy effects on the material structure and properties as well as designing advanced electrocatalysts.

CRedit authorship contribution statement

Meng Zeshuo: Conceptualization, Data curation, Methodology, Writing – original draft, Writing – review & editing. **Zeng Fanda:** Data

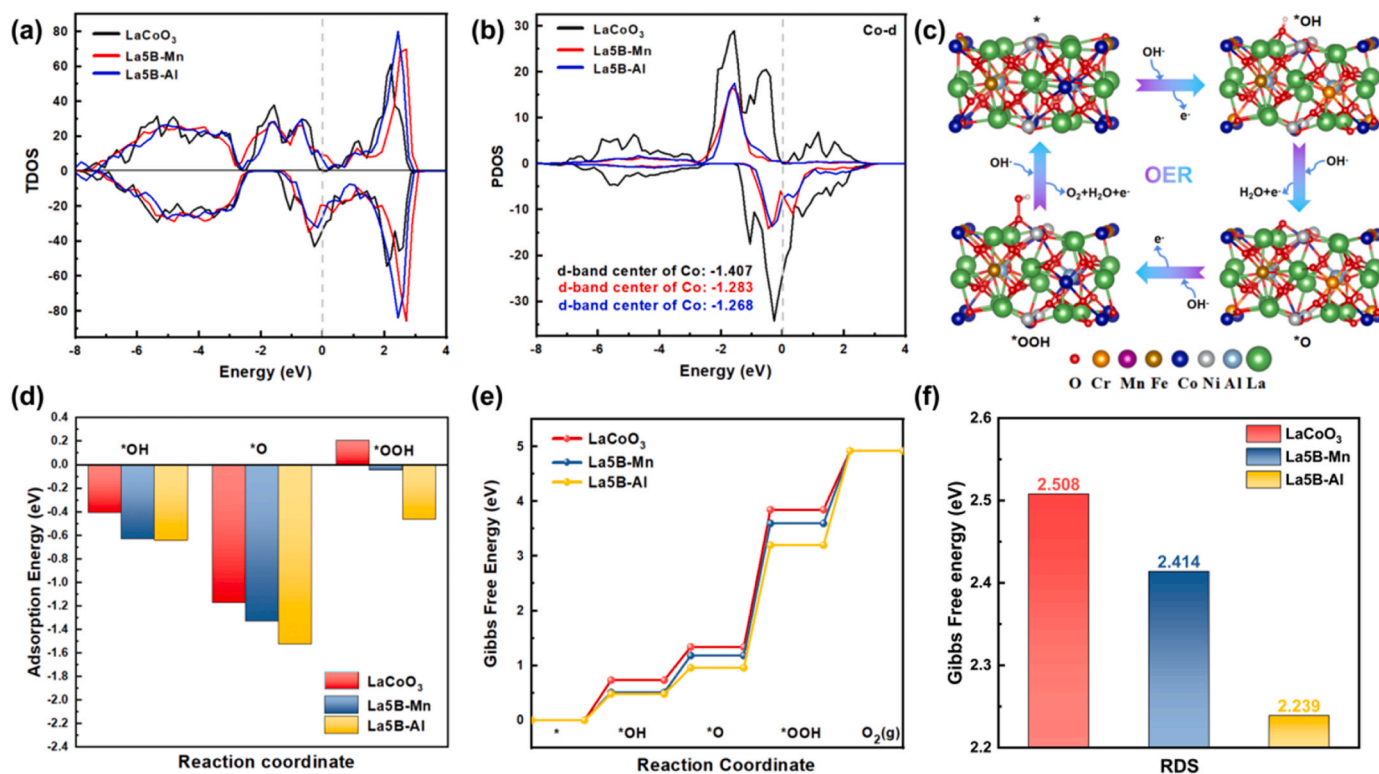


Fig. 6. a) TDOS comparison between LaCoO₃, La5B-Mn, and La5B-Al. b) PDOS of Co-3d. c) Schematic of the OER mechanism on the La5B-Al surface. d) Adsorption energy of the intermediates. e) Gibbs free energy diagram of the OER at the Co sites on the LaCoO₃, La5B-Mn, and La5B-Al surfaces. f) Gibbs free energy values of the RDS.

curation, Investigation. **Hu Xiaoying:** Methodology, Project administration. **Tian Hongwei:** Resources, Software. **Xu Zijin:** Conceptualization, Formal analysis, Methodology, Writing – original draft. **Zhang Runlin:** Conceptualization, Validation. **Du Zhengyan:** Investigation, Methodology, Software, Writing – original draft.

Declaration of Competing Interest

The authors declare that they have no known competing financial interests or personal relationships that could have appeared to influence the work reported in this paper.

Data Availability

Data will be made available on request.

Acknowledgements

This work was supported by the Scientific and Technological Development Program of Jilin Province (20220201138GX).

Appendix A. Supporting information

Supplementary data associated with this article can be found in the online version at [doi:10.1016/j.apcatb.2023.123668](https://doi.org/10.1016/j.apcatb.2023.123668).

References

- [1] J. Song, C. Wei, Z.-F. Huang, C. Liu, L. Zeng, X. Wang, Z.-J. Xu, A review on fundamentals for designing oxygen evolution electrocatalysts, *Chem. Soc. Rev.* 49 (2020) 2196–2214.
- [2] Z.-F. Huang, J. Wang, Y. Peng, C.-Y. Jung, A. Fisher, X. Wang, Design of efficient bifunctional oxygen reduction/evolution electrocatalyst: recent advances and perspectives, *Adv. Energy Mater.* 7 (2017), 1700544.
- [3] L.A. King, M.A. Hubert, C. Capuano, J. Manco, N. Danilovic, E. Valle, T. R. Hellstern, K. Ayers, T.F. Jaramillo, A non-precious metal hydrogen catalyst in a commercial polymer electrolyte membrane electrolyser, *Nat. Nanotechnol.* 14 (2019) 1071–1074.
- [4] L. Hou, Z. Li, H. Jang, Y. Wang, X. Cui, X. Gu, M.G. Kim, L. Feng, S. Liu, X. Liu, Electronic and lattice engineering of ruthenium oxide towards highly active and stable water splitting, *Adva. Energy Mater.* 13 (2023), 2300177.
- [5] Z.-Q. Liu, K. Xiao, Y. Wang, P. Wu, L. Hou, Activating lattice oxygen in spinel ZnCo₂O₄ through filling the oxygen vacancies with fluorine for electrocatalytic oxygen evolution, *Angew. Chem. (Int. Ed. Engl.)* (2023) e202301408-e202301408.
- [6] Y. Li, Y. Wu, T. Li, M. Lu, Y. Chen, Y. Cui, J. Gao, G. Qian, Tuning the electronic structure of a metal-organic framework for an efficient oxygen evolution reaction by introducing minor atomically dispersed ruthenium, *Carbon Energy* 5 (2023), <https://doi.org/10.1002/cey2.265>.
- [7] Z.-P. Wu, X.F. Lu, S.-Q. Zang, X.W. Lou, Non-noble-metal-based electrocatalysts toward the oxygen evolution reaction, *Adv. Funct. Mater.* 30 (2020), 1910274.
- [8] X. Xu, Y. Pan, L. Ge, Y. Chen, X. Mao, D. Guan, M. Li, Y. Zhong, Z. Hu, V. K. Peterson, M. Saunders, C.-T. Chen, H. Zhang, R. Ran, A. Du, H. Wang, S.P. Jiang, W. Zhou, Z. Shao, High-performance perovskite composite electrocatalysts enabled by controllable interface engineering, *Small* 17 (2021), 2101573.
- [9] J.T. Mefford, W.G. Hardin, S. Dai, K.P. Johnston, K.J. Stevenson, Anion charge storage through oxygen intercalation in LaMnO₃ perovskite pseudocapacitor electrodes, *Nat. Mater.* 13 (2014) 726–732.
- [10] J. He, X. Xu, M. Li, S. Zhou, W. Zhou, Recent advances in perovskite oxides for non-enzymatic electrochemical sensors: a review, *Anal. Chim. Acta* 1251 (2023), 341007.
- [11] J. Ran, L. Wang, M. Si, X. Liang, D. Gao, Tailoring spin state of perovskite oxides by fluorine atom doping for efficient oxygen electrocatalysis, *Small* 19 (2022), 2206367.
- [12] X.M. Xu, C. Su, Z.P. Shao, Fundamental understanding and application of Ba_{0.5}Sr_{0.5}Co_{0.8}Fe_{0.2}O_{3-δ} perovskite in energy storage and conversion: past, present, and future, *Energy Fuels* 35 (2021) 13585–13609.
- [13] H. Li, J. Yu, Y. Gong, N. Lin, Q. Yang, X. Zhang, Y. Wang, Perovskite catalysts with different dimensionalities for environmental and energy applications: a review, *Sep. Purif. Technol.* 307 (2023), 122716.
- [14] X. Xu, W. Wang, W. Zhou, Z. Shao, Recent advances in novel nanostructuring methods of perovskite electrocatalysts for energy-related applications, *Small Methods* 2 (2018), 1800071.
- [15] K.-X.Z. Xiao Liang, Yu-Cheng Shen, Ke Sun, Lei Shi, Hui Chen, Ke-Yan Zheng, Xiao-Xin Zou, Perovskite-type water oxidation electrocatalysts, *J. Electrochem.* 28 (2022), 2214004.

- [16] Y. Xin, S. Li, Y. Qian, W. Zhu, H. Yuan, P. Jiang, R. Guo, L. Wang, High-entropy alloys as a platform for catalysis: progress, challenges, and opportunities, *ACS Catal.* 10 (2020) 11280–11306.
- [17] A. Sarkar, Q. Wang, A. Schiele, M.R. Chellali, S.S. Bhattacharya, D. Wang, T. Brezesinski, H. Hahn, L. Velasco, B. Breitung, High-entropy oxides: fundamental aspects and electrochemical properties, *Adv. Mater.* 31 (2019), 1806236.
- [18] X. Xu, Z. Shao, S.P. Jiang, High-entropy materials for water electrolysis, *Energy Technol.* 10 (2022), 2200573.
- [19] Z. Meng, X. Gong, J. Xu, X. Sun, F. Zeng, Z. Du, Z. Hao, W. Shi, S. Yu, X. Hu, H. Tian, A general strategy for preparing hollow spherical multilayer structures of oxygen-rich vacancy transition metal oxides, especially high entropy perovskite oxides, *Chem. Eng. J.* 457 (2023), 141242.
- [20] B. Zhao, Y. Du, Z. Yan, L. Rao, G. Chen, M. Yuan, L. Yang, J. Zhang, R. Che, Structural defects in phase-regulated high-entropy oxides toward superior microwave absorption properties, *Adv. Funct. Mater.* 33 (2023), 2209924.
- [21] S. Akrami, P. Edalati, M. Fujii, K. Edalati, High-entropy ceramics: review of principles, production and applications, *Mater. Sci. Eng. R.-Rep.* 146 (2021), 100644.
- [22] N. Thi Xuyen, Y.-C. Liao, C.-C. Lin, Y.-H. Su, J.-M. Ting, Advanced high entropy perovskite oxide electrocatalyst for oxygen evolution reaction, *Adv. Funct. Mater.* 31 (2021), 2101632.
- [23] J.H. Montoya, L.C. Seitz, P. Chakthranont, A. Vojvodic, T.F. Jaramillo, J. K. Nørskov, Materials for solar fuels and chemicals, *Nat. Mater.* 16 (2017) 70–81.
- [24] G. Kresse, J. Hafner, Ab initio molecular dynamics for liquid metals, *Phys. Rev. B* 47 (1993) 558–561.
- [25] G. Kresse, J. Furthmüller, Efficient iterative schemes for ab initio total-energy calculations using a plane-wave basis set, *Phys. Rev. B* 54 (1996) 11169–11186.
- [26] J.P. Perdew, K. Burke, M. Ernzerhof, Generalized gradient approximation made simple, *Phys. Rev. Lett.* 77 (1996) 3865–3868.
- [27] P.E. Blöchl, Projector augmented-wave method, *Phys. Rev. B* 50 (1994) 17953–17979.
- [28] S. Grimme, J. Antony, S. Ehrlich, H. Krieg, A consistent and accurate ab initio parametrization of density functional dispersion correction (DFT-D) for the 94 elements H-Pu, *J. Chem. Phys.* 132 (2010), 154104.
- [29] A. Reuss, Berechnung der fließgrenze von mischkristallen auf grund der plastizitätsbedingung für einkristalle, *ZAMM - J. Appl. Math. Mech. / Z. für Angew. Math. und Mech.* 9 (1929) 49–58.
- [30] R. Hill, The elastic behaviour of a crystalline aggregate, *Proc. Phys. Soc. Sect. A* 65 (1952) 349.
- [31] J.K. Nørskov, J. Rossmeisl, A. Logadottir, L. Lindqvist, J.R. Kitchin, T. Bligaard, H. Jónsson, Origin of the overpotential for oxygen reduction at a fuel-cell cathode, *J. Phys. Chem. B* 108 (2004) 17886–17892.
- [32] K. Liu, H. Jin, L. Huang, Y. Luo, Z. Zhu, S. Dai, X. Zhuang, Z. Wang, L. Huang, J. Zhou, Puffing ultrathin oxides with nonlayered structures, *Sci. Adv.* 8 (2022), eabn2030.
- [33] H. Jia, M. Horton, Y. Wang, S. Zhang, K.A. Persson, S. Meng, M. Liu, Persona of transition metal ions in solids: a statistical learning on local structures of transition metal oxides, *Adv. Sci.* 9 (2022), 2202756.
- [34] Z.-Y. Yu, Y. Duan, Y. Kong, X.-L. Zhang, X.-Y. Feng, Y. Chen, H. Wang, X. Yu, T. Ma, X. Zheng, J. Zhu, M.-R. Gao, S.-H. Yu, General synthesis of tube-like nanostructured perovskite oxides with tunable transition metal-oxygen covalency for efficient water electrooxidation in neutral media, *J. Am. Chem. Soc.* 144 (2022) 13163–13173.
- [35] Y. Wu, F. Zhang, X. Yuan, H. Huang, X. Wen, Y. Wang, M. Zhang, H. Wu, X. Liu, H. Wang, S. Jiang, Z. Lu, Short-range ordering and its effects on mechanical properties of high-entropy alloys, *J. Mater. Sci. Technol.* 62 (2021) 214–220.
- [36] M. Sivakumar, M. Sakthivel, S.-M. Chen, P. Veerakumar, S.-B. Liu, Sol-gel synthesis of carbon-coated LaCoO₃ for effective electrocatalytic oxidation of salicylic acid, *Chemelectrochem* 4 (2017) 935–940.
- [37] L. Wang, Q. Pang, Q. Song, X. Pan, L. Jia, Novel microbial synthesis of Cu doped LaCoO₃ photocatalyst and its high efficient hydrogen production from formaldehyde solution under visible light irradiation, *Fuel* 140 (2015) 267–274.
- [38] Y. Wang, L. Yu, R. Wang, Y. Wang, X. Zhang, Reactivity of carbon spheres templated Ce/LaCo_{0.5}Cu_{0.5}O₃ in the microwave induced H₂O₂ catalytic degradation of salicylic acid: characterization, kinetic and mechanism studies, *J. Colloid Interface Sci.* 574 (2020) 74–86.
- [39] A. Worayingyong, P. Kangvansura, S. Ausadasuk, P. Praserttham, The effect of preparation: Pechini and Schiff base methods, on adsorbed oxygen of LaCoO₃ perovskite oxidation catalysts, *Colloids Surf. A-Physicochem. Eng. Asp.* 315 (2008) 217–225.
- [40] L. Tang, Y. Yang, H. Guo, Y. Wang, M. Wang, Z. Liu, G. Yang, X. Fu, Y. Luo, C. Jiang, Y. Zhao, Z. Shao, Y. Sun, High configuration entropy activated lattice oxygen for O₂ formation on perovskite electrocatalyst, *Adv. Funct. Mater.* 32 (2022), 2112157.
- [41] L. Zhang, J.M.A. Fischer, Y. Jia, X. Yan, W. Xu, X. Wang, J. Chen, D. Yang, H. Liu, L. Zhuang, M. Hankel, D.J. Searles, K. Huang, S. Feng, C.L. Brown, X. Yao, Coordination of atomic Co-Pt coupling species at carbon defects as active sites for oxygen reduction reaction, *J. Am. Chem. Soc.* 140 (2018) 10757–10763.
- [42] Z. Zhuang, Y. Li, Y. Li, J. Huang, B. Wei, R. Sun, Y. Ren, J. Ding, J. Zhu, Z. Lang, L. V. Moskaleva, C. He, Y. Wang, Z. Wang, D. Wang, Y. Li, Atomically dispersed nonmagnetic electron traps improve oxygen reduction activity of perovskite oxides, *Energy Environ. Sci.* 14 (2021) 1016–1028.
- [43] W. Yang, Z. Han, G. Zheng, The influences of lattice distortion on the antiferroelectric transition and relaxation of oxygen vacancies in high-entropy perovskites (Bi_{0.2}Na_{0.2}Ba_{0.2}K_{0.2}X_{0.2})TiO₃ with X=Ca, Sr or La, *Scr. Mater.* 203 (2021), 114096.
- [44] J. Dabrowa, A. Olszewska, A. Falkenstein, C. Schwab, M. Szymczak, M. Zajusz, M. Mozdierz, A. Mikula, K. Zielinska, K. Berent, T. Czeppe, M. Martin, K. Swierczek, An innovative approach to design SOFC air electrode materials: high entropy La_{1-x}Sr_x(Co,Cr,Fe,Mn,Ni)O_{3-delta} (x=0, 0.1, 0.2, 0.3) perovskites synthesized by the sol-gel method, *J. Mater. Chem. A* 8 (2020) 24455–24468.
- [45] T.G. Ritter, A.H. Phakatkar, M.G. Rasul, M.T. Saray, L.V. Sorokina, T. Shokuhfar, J. M. Goncalves, R. Shabbazian-Yassar, Electrochemical synthesis of high entropy hydroxides and oxides boosted by hydrogen evolution reaction, *Cell Rep. Phys. Sci.* 3 (2022), 100847.
- [46] T. Liang, X. Zhang, L. Su, R. Hou, B. Yang, J. Lang, S. Yang, X. Yan, Superiority of cubic perovskites oxides with strong B-O hybridization for oxygen-anion intercalation pseudocapacitance, *Adv. Funct. Mater.* 32 (2022), 2202245.
- [47] S. Hu, W.-X. Li, Sabatier principle of metal-support interaction for design of ultrastable metal nanocatalysts, *Science* 374 (2021) 1360–1365.
- [48] J. Zhao, Z. Li, M. Wang, Q. Wang, Z. Jin, Exploring the film growth in perovskite solar cells, *J. Mater. Chem. A* 9 (2021) 6029–6049.
- [49] J.-C. Liu, L. Luo, H. Xiao, J. Zhu, Y. He, J. Li, Metal affinity of support dictates sintering of gold catalysts, *J. Am. Chem. Soc.* 144 (2022) 20601–20609.
- [50] Q. Zhang, Y. Zhang, H. Wu, X. Zhao, M. Wang, S. Wang, R. Feng, Q. Chen, F. Song, M. Chen, P. Liu, Entropy-stabilized multicomponent porous spinel nanowires of NiFe_xO₄ (X = Fe, Ni, Al, Mo, Co, Cr) for efficient and durable electrocatalytic oxygen evolution reaction in alkaline medium, *ACS Nano* 17 (2023) 1485–1494.
- [51] N.W. Ashcroft, Solid state physics [by] Neil W. Ashcroft [and] N. David Mermin, 1976.
- [52] C. Kittel, Introduction to solid state physics / by Charles Kittel, 1976.
- [53] Y. Zheng, L. Wang, H. Liu, J. Yang, R. Zhang, L. Zhang, Z.-A. Qiao, A modular co-assembly strategy for ordered mesoporous perovskite oxides with abundant surface active sites, *Angew. Chem. -Int. Ed.* 61 (2022), 2209038.
- [54] Q.F. He, J.G. Wang, H.A. Chen, Z.Y. Ding, Z.Q. Zhou, L.H. Xiong, J.H. Luan, J. M. Pelletier, J.C. Qiao, Q. Wang, L.L. Fan, Y. Ren, Q.S. Zeng, C.T. Liu, C.W. Pao, D. J. Srolovitz, Y. Yang, A highly distorted ultraelastic chemically complex Elinvar alloy, *Nature* 603 (2022) 251–257.
- [55] Y. Zhai, X. Ren, B. Wang, S. Liu, High-entropy catalyst-a novel platform for electrochemical water splitting, *Adv. Funct. Mater.* 32 (2022), 2207536.
- [56] C. Chen, Y. Tuo, Q. Lu, H. Lu, S. Zhang, Y. Zhou, J. Zhang, Z. Liu, Z. Kang, X. Feng, D. Chen, Hierarchical trimetallic Co-Ni-Fe oxides derived from core-shell structured metal-organic frameworks for highly efficient oxygen evolution reaction, *Appl. Catal. B-Environ.* 287 (2021), 119953.
- [57] A. Abdelhafiz, B. Wang, A.R. Harutyunyan, J. Li, Carbothermal shock synthesis of high entropy oxide catalysts: dynamic structural and chemical reconstruction boosting the catalytic activity and stability toward oxygen evolution reaction, *Adv. Energy Mater.* 12 (2022), 2200742.
- [58] H. Zheng, Y. Zhang, Y. Wang, Z. Wu, F. Lai, G. Chao, N. Zhang, L. Zhang, T. Liu, Perovskites with enriched oxygen vacancies as a family of electrocatalysts for efficient nitrate reduction to ammonia, *Small* 19 (2022), 2205625.
- [59] Z. Xu, Y. Wu, X. Wang, Q. Ji, T. Li, H. He, H. Song, S. Yang, S. Li, S. Yan, L. Zhang, Z. Zou, Identifying the role of oxygen vacancy on cobalt-based perovskites towards peroxymonosulfate activation for efficient iohexol degradation, *Appl. Catal. B: Environ.* 319 (2022), 121901.
- [60] J. Li, F. Yang, M. Jiang, X. Cai, Q. Hu, J. Zhang, The critical role of A, B-site cations and oxygen vacancies on the OER electrocatalytic performances of Bi_(0.15)Sr_(0.85)Co_(1-x)Fe_xO_(3-d) (0.2=x=1) perovskites in alkaline media, *Chem. Eng. J.* 451 (2023), 138646.
- [61] F. Bertella, C.W. Lopes, A.C. Foucher, G. Agostini, P. Concepción, E.A. Stach, A. Martínez, Insights into the promotion with Ru of Co/TiO₂ Fischer-Tropsch catalysts: an in situ spectroscopic study, *ACS, ACS Catal.* 10 (2020) 6042–6057.
- [62] W. Hooch Antink, S. Lee, H.S. Lee, H. Shin, T.Y. Yoo, W. Ko, J. Shim, G. Na, Y.-E. Sung, T. Hyeon, High-valence metal-driven electronic modulation for boosting oxygen evolution reaction in high-entropy spinel oxide, *Adv. Funct. Mater.* (2023), 2309438.
- [63] W. Guo, L. Cui, H. Xu, C. Gong, Selective dissolution of A-site cations of La_{0.6}Sr_{0.4}Co_{0.8}Fe_{0.2}O₃ perovskite catalysts to enhance the oxygen evolution reaction, *Appl. Surf. Sci.* 529 (2020), 147165.
- [64] W. Li, S. Xia, Z. Wang, B. Zhang, B. Li, L. Zhang, K. Qian, J. Ma, X. He, Covalency competition triggers Fe-Co synergistic catalysis for boosted Fenton-like reactions, *Appl. Catal. B: Environ.* 325 (2023), 122358.
- [65] N. Li, R.G. Hadt, D. Hayes, L.X. Chen, D.G. Nocera, Detection of high-valent iron species in alloyed oxidic cobaltates for catalysing the oxygen evolution reaction, *Nat. Commun.* 12 (2021) 4218.
- [66] Y.V. Kaneti, Y. Guo, N.L.W. Septiani, M. Iqbal, X. Jiang, T. Takei, B. Yuliarto, Z. A. Allothman, D. Golberg, Y. Yamauchi, Self-templated fabrication of hierarchical hollow manganese-cobalt phosphide yolk-shell spheres for enhanced oxygen evolution reaction, *Chem. Eng. J.* 405 (2021), 126580.
- [67] H. Nan, S. Lv, Z. Xu, Y. Feng, Y. Zhou, M. Liu, T. Wang, X. Liu, X. Hu, H. Tian, Inducing the cocktail effect in yolk-shell high-entropy perovskite oxides using an electronic structural design for improved electrochemical applications, *Chem. Eng. J.* 452 (2023), 139501.
- [68] X. Zheng, J. Yang, Z. Xu, Q. Wang, J. Wu, E. Zhang, S. Dou, W. Sun, D. Wang, Y. Li, Ru-Co pair sites catalyst boosts the energetics for the oxygen evolution reaction, *Angew. Chem. Int. Ed.* 61 (2022), 2205946.

- [69] S. Wan, J. Xu, S. Cao, J. Yu, Promoting intramolecular charge transfer of graphitic carbon nitride by donor–acceptor modulation for visible-light photocatalytic H₂ evolution, *Interdiscip. Mater.* 1 (2022) 294–308.
- [70] C. Zhong, J. Zhang, L. Zhang, Y. Tu, L. Du, Z. Cui, H. Song, Composition-tunable Co_{3–x}Fe_xMo₃N electrocatalysts for the oxygen evolution reaction, *ACS Energy Lett.* 8 (2023) 1455–1462.
- [71] S. Wen, J. Huang, T. Li, W. Chen, G. Chen, Q. Zhang, X. Zhang, Q. Qian, K. Ostrikov, Multiphase nanosheet-nanowire cerium oxide and nickel-cobalt phosphide for highly-efficient electrocatalytic overall water splitting, *Appl. Catal. B: Environ.* 316 (2022), 121678.